

Tactile-based Exploration, Mapping and Navigation with Collision-Resilient Aerial Vehicles

Karishma Patnaik, Aravind Adhith Pandian Saravanakumaran and Wenlong Zhang*

Abstract—In this article, we introduce novel tactile-based motion primitives termed “tactile-traversal”, “tactile-turning” and “ricocheting” for unmanned aerial vehicles (UAVs). These primitives enable contact-rich UAV missions such as tactile-based exploration, mapping, and collision-inclusive navigation. We begin by introducing XPLOER, a passive deformable UAV that sustains collisions and establishes smooth contacts by exploiting its spring-augmented chassis. Next, an improved and fast converging external force estimation algorithm is proposed to detect contacts/collisions. We also design three distinct reaction controllers for (i) static-wrench application, (ii) disturbance rejection, and (iii) collision recovery. Finally, the three new tactile-based motion primitives are proposed by leveraging the reactions obtained from deploying these controllers to interact with surroundings. We showcase the effectiveness of these primitives to facilitate efficient exploration and rapid navigation in unknown environments by capitalizing on collisions and contacts.

I. INTRODUCTION

Unmanned aerial vehicles (UAVs) have been extensively employed in manipulation and for physical interaction tasks such as grasping, perching, and pushing/pulling [1], [2]. Conventional UAVs accomplish these tasks by the use of additional manipulators [3]–[5]. While research with such augmented platforms has shown great promise, it is understood that reconfigurability and mechanical intelligence of a UAV chassis can beget versatility, improve flight efficiency, and enable safe interaction, all at once [6], [7]. A majority of such reconfigurable UAVs, however, have active actuation mechanisms for initiating a change in their morphology, classified as *active* morphing UAVs, and require attention to meticulous planning [8]. In contrast, when the UAV reacts to external physical forces and undergoes a change in morphology, we call it a *passive* morphing UAV [9]. For such vehicles, collision energies are harnessed to initiate deformation using various materials and structures such as springs, foldable origami, and inflatable textiles [10]–[13]. This article aims to demonstrate the benefits of the collision-resilient, passive morphing UAVs to perform physical interaction tasks by proposing new specially tailored, contact-based algorithms.

A. Related Literature

1) *External Wrench Estimation*: Augmenting a UAV with force-torque sensors to detect external wrench increases the total weight of the aerial vehicle platform and adversely

The authors are with School of Manufacturing Systems and Networks, Ira A. Fulton Schools of Engineering, Arizona State University, Mesa, AZ, 85212, USA. Email: {kpatnaik, apandian, wenlong.zhang}@asu.edu.

*Address all correspondence to this author.

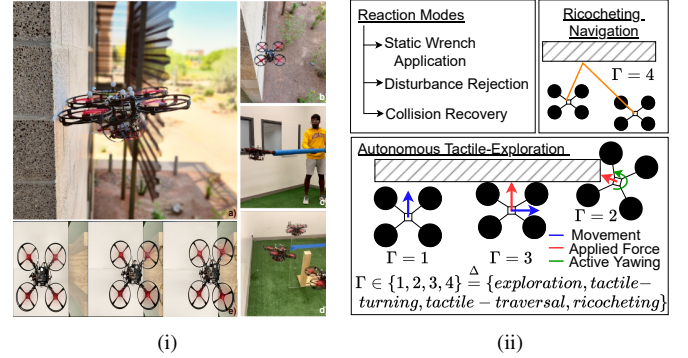


Fig. 1. (i) An overview of XPLOER performing various aerial-physical interaction and contact-rich tasks with a sequence of slow-motion snapshots highlighting the deformation of XPLOER’s chassis for smooth contacts. (ii) Primitive $\Gamma \in \{1, 2, 3, 4\}$ for tactile-based exploration and navigation.

affects flight time [14], [15]. Alternatively, researchers have developed algorithms based on momentum-based [16], [17] and acceleration-based [18], [19] wrench estimators which rely on only the available onboard sensors such as inertial measurement units (IMUs). Other Kalman-filter based approaches and hybrid methods were proposed in [20], [21] for conventional UAVs. For this work, we aim to utilize proprioceptive information about the vehicle’s morphology to identify contact and generate an accurate force estimate.

2) *Static Force Application and Tactile-based Inspection*: Using the external wrench estimate, UAVs can now be pursued for performing tactile-based tasks such as non-destructive testing, vibration analysis, and leak identification which require a desired wrench to be applied onto a surface in an attempt to reduce safety risks to human workers [22]–[26]. In this context, we propose to employ soft deformable quadrotors to establish smooth contacts and simplify the contact laws [27].

3) *Tactile-based Navigation*: Collision-resilient designs hold a strong potential for a paradigm shift for performing tactile-based navigation [28]–[32]. This also is an effective way to reduce weight from the additional sensors that can adversely affect flight time. A planner for tactile-based navigation was proposed in [33] consisting of two modes, sliding and flying cartwheel. Authors of [34] utilized vision systems to navigate manhole-sized tubes along with flaps to sense contacts. In [35] collisions were exploited for path planning using sampling-based methods. However, all the works assume complete knowledge of the map of the environment a-priori. Autonomous navigation in an unknown environment is still nascent and remains an open problem.

4) *Mapping*: Conventionally, mapping an environment is performed by using cameras and Structure from Motion (SfM)

technique [36] by recreating a 3D structure from a series of images captured from different angles. Research carried out in [37] used the combination of cameras, LiDAR, IMU, and encoders to generate a highly precise map of the environment. Another map generation methodology was presented in [21] where collision detection and localization were used to insert obstacle blocks into the point cloud map. However, autonomous planning for performing these missions accurately in unknown low-visible environments where collisions are inevitable still remains a challenge.

B. Contributions of Present Work

This article aims to explore further benefits of the passive reconfigurable quadrotors for performing contact-rich tasks such as exploration, navigation, and mapping. The advantage of having a deformable chassis makes passive reconfigurable UAVs ideal candidates to make, break, or sustain repeated contacts without exhaustive hybrid control strategies. The main contributions of the article are:

- 1) Development of an external force estimation algorithm for the deformable quadrotor, XPLOER.
- 2) Propose and develop new tactile exploration primitives (*Tactile-traversal*, *Tactile-turning*) for passive deformable UAVs to explore unknown flight spaces.
- 3) Develop a pipeline to create accurate maps of previously unknown environments through autonomous tactile-based exploration.
- 4) Propose and develop a *Ricocheting* primitive for way-point tracking in minimum time by leveraging collision energy dissipation.

Figure 1 and Supplementary Video 1 showcases our compliant and passive deformable quadrotor, XPLOER, engaged in various contact-rich tasks. The rest of the article is structured as follows: Section II provides an overview of the design and low-level control of XPLOER. In Section III-A, we introduce the external force estimation algorithm, and Section III-B introduces three reaction modes upon contact. Section IV presents three new tactile-based missions and Section V presents the results in real-world implementations. Finally, Section VI concludes the article.

II. DESIGN AND LOW-LEVEL CONTROL OF XPLOER

In this work, we use a modified version of the passive foldable aerial robot from our previous work [10]. Built on a similar idea, XPLOER (shown in Fig. 1) has four deformable arms as part of its morphing chassis, however, all four motors lie in a single plane. The springs chosen for the current version are stiffer than our previous design to ensure that the collision-induced deformation is induced in a smaller range of 30° . This design choice was made for two specific reasons, with the first being that we wanted to lower the height of the center of mass (CoM) from our previous design to prevent toppling when making contact with the environment. This is shown in Fig. 1(e) where the deformation of the chassis easily allows large forces around 1N to be exerted on the environment without pitching into the wall, unlike the rigid conventional chassis. Secondly, we need to ensure that the vehicle will not get stuck in corner cases during exploration and hence redesigned the

TABLE I

Symbol	Definition
$\mathbf{x} \in \mathbb{R}^3$	3D position of the system
$\mathbf{v} \in \mathbb{R}^3$	3D translational velocity of the system
$\mathbf{R} \in \mathbb{R}^{3 \times 3}$	rotation matrix
$\mathbf{H} \in \mathbb{R}^{3 \times 3}$	inertia matrix of system, assumed constant
\mathcal{O}_w	vehicle geometric center
${}_w\mathcal{F} = \{\mathbf{e}_1, \mathbf{e}_2, \mathbf{e}_3\}$	inertial frame
${}_b\mathcal{F} = \{\mathbf{b}_1, \mathbf{b}_2, \mathbf{b}_3\}$	body fixed frame
$\theta_i \in \mathbb{R}$	angle made by the i^{th} arm with the b_2 axis. This follows the right-hand rule
$(\cdot)(\bullet)$	denotes the quantity (\bullet) in the (\cdot) frame
$\mathbf{a}_i \mathcal{F} = \{\mathbf{a}_1^i, \mathbf{a}_2^i\}$	i^{th} arm frame with $\mathbf{a}_j^i \forall j = 1, 2$ denoting the basis vectors for the i^{th} frame
$k \in \mathbb{R}, b \in \mathbb{R}$	stiffness and damping coefficient for the arm
$\hat{\delta}_a^i \in \mathbb{R}^6$	estimated wrench from spring action at i^{th} arm
$\hat{\delta}_f^i \in \mathbb{R}^3$	estimated net force at the i^{th} arm
$\mathbf{C}_n \in \mathbb{R}^4$	contact normal to the obstacle
$\lambda \in \mathbb{R}$	current move direction of the vehicle
$d_{step} \in \mathbb{R}$	distance to move for each step
$\dot{\psi}_0 \in \mathbb{R}$	yaw rate threshold
$\dot{\psi}_c \in \mathbb{R}$	<i>Tactile-turning</i> yaw rate
$\delta_0 \in \mathbb{R}$	force threshold for exploration
$\delta_{\psi_0} \in \mathbb{R}$	force threshold for <i>Tactile-turning</i>
$f_{des} \in \mathbb{R}$	force to be applied on the obstacle
$\delta_{map} \in \mathbb{R}$	force threshold for mapping
$\Upsilon \in \mathbb{R}$	indicates if a contact is made by using the arm angle deviation information

propeller guards, so a maximum of 30° of free rotation was obtained as a result.

The control block diagram is shown in Fig. 2 with the coordinate frame and symbols elaborated in Table I and in Fig. 3. The rigid-body dynamics can be written as:

$$\dot{\mathbf{x}} = \mathbf{v}$$

$$m\dot{\mathbf{v}} = m\mathbf{g}\mathbf{e}_3 - f\mathbf{R}\mathbf{e}_3 + \delta_f \quad (1a)$$

$$\dot{\mathbf{R}} = \mathbf{R}\hat{\Omega}$$

$$\mathbf{H}\dot{\hat{\Omega}} - [\mathbf{H}\hat{\Omega}]_{\times}\hat{\Omega} = \boldsymbol{\tau} + \delta_{\boldsymbol{\tau}} \quad (1b)$$

where m denotes the mass of the vehicle, and $\mathbf{x} \in \mathbb{R}^3$ and $\mathbf{v} \in \mathbb{R}^3$ denote the position and translational velocity of the vehicle, respectively. The other symbols and definitions adhere to literature [10]. Please see Appendix for details. The terms $\delta_f \in \mathbb{R}^3$ and $\delta_{\boldsymbol{\tau}} \in \mathbb{R}^3$ denote the lumped external forces and torques respectively applied on the system. The *hat map* $\hat{\cdot} : \mathbb{R}^3 \rightarrow \text{SO}(3)$ is a symmetric matrix operator defined by the condition that $\hat{\mathbf{x}}\mathbf{y} = \mathbf{x} \times \mathbf{y} \forall \mathbf{x}, \mathbf{y} \in \mathbb{R}^3$ and $[\cdot]_{\times}$ is the skew symmetric cross product matrix. The rest of the nomenclature is given in Table I. A cascaded P-PID controller is employed for both the position and attitude loops of the low-level controller for XPLOER as shown in Fig. 2 with the errors defined on position and quaternion space respectively. The arm angle deviations for the collision tests and flight tests conducted induced a change of about 10° which produces small inertia deflections, to which the employed P-PID structure of the low-level controller is inherently robust.

III. EXTERNAL FORCE ESTIMATION AND REACTION

We propose a novel force estimator by fusing together the estimates from the proprioceptive state of the arm angles with the one from the IMU at the CoM. The frames used are shown in Fig. 3 and the external wrench $[\delta_f \ \delta_{\boldsymbol{\tau}}]^T$ is assumed to be in lumped form, as shown in (1a) and (1b).

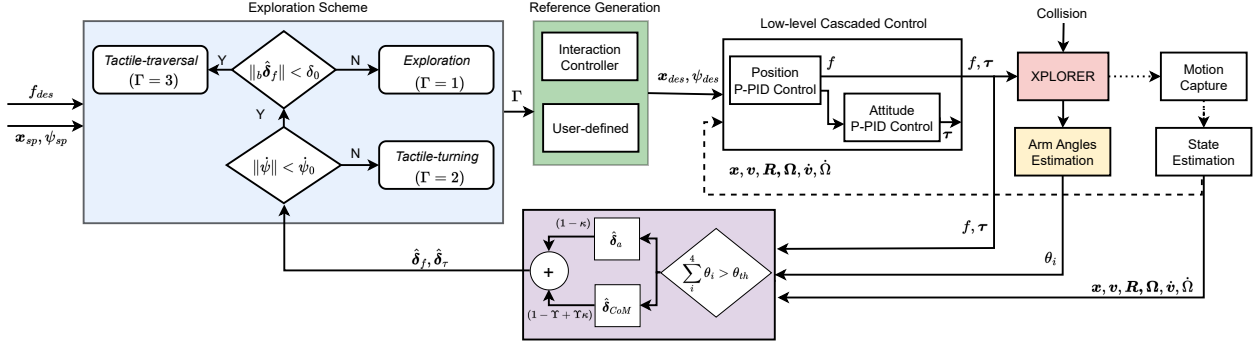


Fig. 2. Complete block diagram for an autonomous exploration task with XPLORER. Collisions and contacts are characterized by the external wrench shown by the purple-shaded block. This value is used to decide the state of exploration (Γ) as shown by the state machine in the blue-shaded block or for navigation. For exploration, Γ is used to generate a suitable reference for position (\mathbf{x}_{des}) and yaw (ψ_{des}).

A. Proposed External Force Estimation Algorithm

1) *Force estimate by the spring action at arm:* The force estimate $\hat{\delta}_{f_{a_i}} \in \mathbb{R}$ from the arm deflection θ_i is derived by modeling the arm dynamics as a torsional spring damper:

$$\mathcal{J}_{zz}\ddot{\theta}_i + b\dot{\theta}_i + k\theta_i = \delta_{\tau_{a_i}} = \delta_{f_{a_i}} l. \quad (2)$$

where \mathcal{J}_{zz} is the inertia of the arm about the z axis, b and k are the damper and spring coefficients respectively and θ_i is the deflection in the angle for the i^{th} arm. The corresponding true external torque is denoted by $\delta_{\tau_{a_i}} \in \mathbb{R}$. We assume that the point of force application on each arm is at the motor location since this is where the CoM of the arm roughly lies (SolidWorks estimate). The true external force is then obtained from $\delta_{\tau_{a_i}}$ by assuming a constant distance l from the motor location to the spring center as shown by Fig. 3. Finally, we employ a first order low-pass filter to estimate $a_i \hat{\delta}_{f_{a_i}}$:

$$a_i \hat{\delta}_{f_{a_i}} = [K_I(\delta_{f_{a_i}} - \hat{\delta}_{f_{a_i}}) 0]^T \quad (3)$$

where $a_i \hat{\delta}_{f_{a_i}} \in \mathbb{R}^2$ denotes the force obtained in the i^{th} arm frame in the a_1^i and a_2^i directions, K_I denotes the filter gain and the $\delta_{f_{a_i}}$ denotes the true external force. Now the external force obtained from the i^{th} arm in the inertial frame can be written as $\hat{\delta}_{f_a}^i \in \mathbb{R}^3 = [{}^w \hat{\delta}_{f_a}^i 0]^T$ with:

$${}^w \hat{\delta}_{f_a}^i = {}^w \mathbf{R}_{a_i}^b \mathbf{R}_{a_i}^i \hat{\delta}_{f_a}^i \quad (4)$$

where ${}^w \mathbf{R}$ denotes the rotation from the body frame to the inertial frame and ${}^b \mathbf{R}$ denotes rotation from the arm frame to the body frame. See Appendix for details.

2) *Force estimate by using IMU at CoM:* Next, following [21], the force information can also be directly estimated from the acceleration measurement of the vehicle from the high-precision IMU in the onboard flight controller. Then, rearranging (1a) and using a median low-pass filter, we obtain:

$$\hat{\delta}_{f_{CoM}} = m\dot{v} - mge_3 + f\mathbf{R} \quad (5)$$

3) *Net Estimated Force on XPLORER:* The external force obtained from the IMU at CoM has a slower convergence rate than the arm-based estimate. Furthermore, if there is no arm deflection from the external force (e.g. when the force is directly applied at CoM), the estimate based on only arm angle feedback doesn't converge to the true force, while the estimate

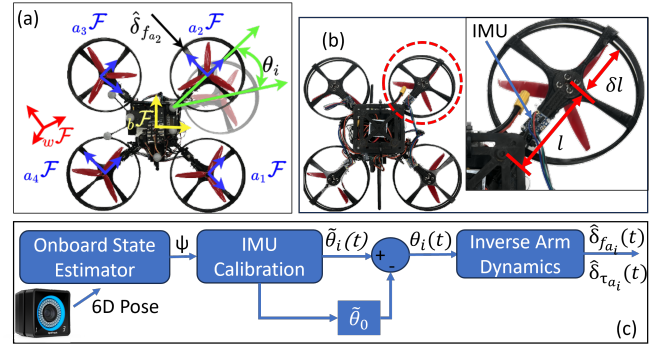


Fig. 3. (a) Frames used to estimate the net external force on each arm, $a_2 \hat{\delta}_{f_{a_2}}$. (b) A zoomed-in view to show the placement of IMU and the assumed point of application of $\hat{\delta}_{f_{a_i}}$. (c) Control block diagram to estimate the $\hat{\delta}_{f_{a_i}}$.

from the CoM is correct in this case. In order to make the best use of the two approaches and obtain a reliable force estimate, we first define an indicator function to detect whether there is contact on the arms as (6):

$$\Upsilon = \begin{cases} 1, & \text{if } \sum_{i=1}^4 |\theta_i| > \theta_{th} \\ 0, & \text{otherwise} \end{cases} \quad (6)$$

where θ_i is the deflection angle of each arm, and θ_{th} is the deflection threshold to detect contact. We now present our external force estimation method $\hat{\delta}_f$ by fusing (3) and (5):

$$\hat{\delta}_f = (1 - \Upsilon + \Upsilon \cdot \kappa_f) \cdot \hat{\delta}_{f_{CoM}} + (1 - \kappa_f) \cdot \Upsilon \cdot \sum_{i=1}^4 \hat{\delta}_{f_{a_i}} \quad (7)$$

where $\kappa_f \in \mathbb{R}^3 = \xi_f \hat{\delta}_{f_{CoM}}$ is an adaptive gain with the tuning parameter ξ_f . $(\bullet)^{| \cdot |}$ denotes element-wise absolute value of the vector (\bullet) . Based on (6) and (7), one gives higher weightage to $\hat{\delta}_{f_{CoM}}$ during collision since the rate of the $\hat{\delta}_{f_{CoM}}$ is higher at the collision instant, so κ_f is larger and the peak from CoM-based estimate is retained. On the other hand, when the wrench estimate from the CoM converges slowly the rate of change is near zero at which instant the term $(1 - \kappa_f)$ is larger, so the total wrench converges to the arm-based estimate.

Finally, a conventional momentum-based torque observer [21] is used with the proposed force estimates to obtain the net external wrench.

B. Reaction Modes and Corresponding Controllers

In this section, the estimated wrench from Section III-A is used to design reaction controllers to get three reaction modes.

1) *Static-wrench application*: Exert a specific force or torque or both on the desired surface. For this case, an admittance controller was designed to maintain a desired interaction wrench. To achieve this goal, we employ standard admittance control strategies [10], [21] and model the desired response as a virtual second-order dynamics:

$$\begin{bmatrix} m_v \mathbf{I}_{3 \times 3} & \mathbf{0}_{3 \times 1} \\ \mathbf{0}_{1 \times 3} & \mathcal{I}_{v,z} \end{bmatrix} \begin{bmatrix} \ddot{\mathbf{r}}_d \\ \ddot{\psi}_d \end{bmatrix} + \mathbf{D} \begin{bmatrix} \dot{\mathbf{r}}_d \\ \dot{\psi}_d \end{bmatrix} + \mathbf{K} \begin{bmatrix} \mathbf{r}_d - \mathbf{r}_d^* \\ \psi_d - \psi_d^* \end{bmatrix} = \begin{bmatrix} \hat{\delta}_f - \delta_{fdes} \\ \hat{\delta}_{\tau_{e,z}} - \delta_{\tau_{des}} \end{bmatrix} \quad (8)$$

where $m_v \in \mathbb{R} > 0$ and $\mathcal{I}_{v,z} \in \mathbb{R} > 0$ are the virtual mass and inertia, $\mathbf{r}_d \in \mathbb{R}^3$ and $\psi_d \in \mathbb{R}$ are the reference position and yaw for the low-level controller. $\mathbf{D} \in \mathbb{R}^{4 \times 4} > 0$ and $\mathbf{K} \in \mathbb{R}^{4 \times 4} > 0$ are the diagonal virtual damping and spring gain matrices, respectively. $\mathbf{r}_d^* \in \mathbb{R}^3$ and $\psi_d^* \in \mathbb{R}$ are the desired setpoints of position and yaw, respectively which are reshaped according to the external wrench. $\hat{\delta}_f$ is the estimated external force, and $\hat{\delta}_{\tau_{e,z}}$ is the current estimated torque about the z -axis (external yaw torque). The complete control block diagram with the interaction controller for XPLOER is shown in Fig. 2. This reaction mode is used to enter the *Tactile-traversal* and *Tactile-turning* states to perform tactile-based exploratory missions as will be detailed in Section IV.

2) *Disturbance rejection*: In this mode, the UAV is commanded to maintain its intended trajectory in the presence of external disturbances. Towards this, the inherent P-PID control structure was exploited for retaining robustness. We employ this mode to perform *Exploration* in free flight as will be detailed later in Section IV.

3) *Collision recovery*: In this mode, we employ a recovery controller to generate a setpoint away from the collision direction, proportional to the collision intensity [12]. We employ this reaction mode to execute novel *Ricocheting* maneuvers as will be described in Section IV.

IV. TACTILE-BASED MOTION PRIMITIVES AND MISSIONS

This section, we present three tactile-based motion primitives (i) *Tactile-turning* (ii) *Tactile-traversal* and (iii) *Ricocheting* which are designed by carefully choosing the parameters of specific reaction modes. We then present the tactile-based exploration, mapping, and swift navigation missions that XPLOER can perform by leveraging these primitives. All the algorithms are written in an algorithmic format in Appendix.

A. Case 1: Tactile-based Exploration

This section describes the exploration scheme for XPLOER to explore its surrounding environment. The algorithm uses an explore-and-exploit strategy, taking advantage of the collision-resilient design and the interaction controller to perform tactile-based navigation. This is achieved through a finite state machine shown in Fig. 2, utilizing, $\hat{\delta}_f \in \mathbb{R}^3$, representing the force estimate in the inertial frame and yaw rate, $\dot{\psi} \in \mathbb{R}$, as inputs to generate the reference trajectory, $[\mathbf{x}_{sp} \ \psi_{sp}]^T$. The exploration strategy is extended from the well-known coverage planning algorithms using a combination of random walk and wall tracing [38]. Further, we employ this exploration scheme for the first time on aerial robots and showcase how it is perfect for exploration with deformable UAVs versus the rigid counterparts due to the benefits of compliance. The workflow of the algorithm is described below.

First, the external force is transformed into the body frame via ${}^b\hat{\delta}_f = {}^b_w \mathbf{R} \hat{\delta}_f$ where ${}^b_w \mathbf{R}$ denotes the rotation matrix from the inertial frame to the body frame. This information is used to update the contact direction flag, $\mathbf{C}_n \in \mathbb{R}^4$, as a vector of four elements with each element representing the direction in body-frame in which the new contact was made, i.e. in $b_1, -b_1, b_2$ or $-b_2$ directions such that $\|\mathbf{C}_n\|_1 = 1$. For example, if $|{}^b\hat{\delta}_{f_x}| > \delta_0$ and ${}^b\hat{\delta}_{f_x} > 0$, \mathbf{C}_n is updated to $[1, 0, 0, 0]$. We also introduce a new variable called the movement direction, λ , which is updated when a new contact is made by using \mathbf{C}_n . The variable λ takes values from the set $\{+X, -X, +Y, -Y\}$ to denote which direction to move for the next exploration step in body frame after an object is detected.

Next, we define three values for the exploration state variable Γ : *Exploration*, *Tactile-turning* and *Tactile-traversal* corresponding to $\Gamma \in \{1, 2, 3\}$ respectively. In obstacle-free flight, XPLOER experiences negligible yaw torques and external forces. We choose this as the trigger condition for entering $\Gamma = 1$, i.e. at any time, if $|\dot{\psi}| < \dot{\psi}_0$ and $|{}^b\hat{\delta}_{f_x}|$ or $|{}^b\hat{\delta}_{f_y}| < \delta_0$, XPLOER switches to the *Exploration* state (Appendix Alg. 1). In this state, the vehicle continues to fly forward in space until it encounters an object in its flight path and generates trajectory setpoints along the body x -axis.

At any given time, we continuously monitor $\dot{\psi}$ to detect turning around a point. This can happen when the vehicle is sliding across the edge of an object by exerting a desired force and at the corner it releases the contact. Since the yaw reference is in admittance, this phenomenon causes the yaw rate to peak instantaneously due to the sudden release. Accordingly we check if $|\dot{\psi}| > \dot{\psi}_0$, where $\dot{\psi}_0$ is the threshold for triggering the *Tactile-turning* (Appendix Alg. 2). In this state, a controlled yaw is generated at a rate of $\dot{\psi}_c$ in the same direction as the detected yaw until $|{}^b\hat{\delta}_{f_x}|$ or $|{}^b\hat{\delta}_{f_y}| > \delta_{\psi_0} \cdot \delta_{\psi_0}$ has to be higher than δ_0 because upon switching to *Tactile-traversal* state the $|{}^b\hat{\delta}_f|$ should be greater than the δ_0 to register contact and update the contact direction \mathbf{C}_n . The threshold $\dot{\psi}_0$ is chosen to be high enough to avoid false triggers of the *Tactile-turning* state. Furthermore, the generated ψ is also limited to 180° to prevent the UAV from yawing indefinitely while ensuring the re-establishment of contact.

The *Tactile-traversal* state (Appendix Alg. 3) allows the XPLOER to traverse obstacles by maintaining contact with the obstacle. In this state, the next exploration direction λ is set parallel to the obstacle plane and towards the right-hand side of the current movement direction to ensure consistent performance. The interaction controller is therefore used to generate $X_{des}(f_{des})$ and $Y_{des}(f_{des})$ in the body frame ensuring that the vehicle maintains contact with the obstacle by exerting a force of $\delta_{f_{des}}$ sideways onto the object while flying forward. In scenarios where XPLOER encounters obstacles in two directions, \mathbf{C}_n is updated with the latest collision direction.

B. Case 2: Tactile-based Mapping

The ability to explore the environment by maintaining contact can be used to generate a map of the obstacle. This synthesized map can be used for motion planning by XPLOER or other autonomous robots. The algorithm utilizes the ${}^b\hat{\delta}_f$, the CAD model of XPLOER, and the global pose

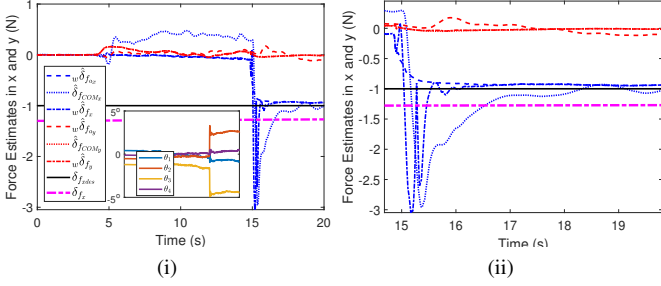


Fig. 4. Results for the force estimation. (i) shows the estimates in inertial x and y axes. The inset shows the corresponding deviation in arm angles. (ii) zoomed-in view of the peak.

to generate the obstacle boundary map. We use the Open3D library [39] for processing the point cloud generated. The overview of the framework is depicted in Appendix Alg. 4.

Obstacle map generation initializes when $|\hat{b}\hat{\delta}_f| \geq \delta_{map}$. δ_{map} is taken to be slightly higher than f_{des} . This choice is to ensure mapping is conducted only when there is firm contact with the obstacle. As an additional condition, the mapping starts if the UAV is flying. The contact normal, C_n , provides the direction of the obstacle, in which an object of dimension $0.25 \text{ m} \times 0.08 \text{ m} \times 0.5 \text{ m}$ is added to the point cloud, offset by 0.21 m from the position of XPLORER. The offset corresponds to the perpendicular distance from XPLORER's center to the edge of each side. In corner cases where the move direction, λ , is not the same as the previous move direction, a fixed point cloud is added diagonally with an offset of 0.417 m to the map to make it continuous around the corners (shown in Supplementary Video 3). The point cloud map is generated at 30 Hz to obtain a high-resolution map of the obstacle. The map is stored as a Polygon File Format (PLY) as per the ASCII format, and it consists of the location of each point in the point cloud. The map generation was done on a computer with AMD Ryzen 5 CPU with 16GB RAM, the ROS2 architecture enabled communication between the high-level companion computer and the offline computer. The map generation relies on the pose of the UAV, which is currently obtained using the motion capture system.

C. Case 3: Ricocheting

In this section, we present a new maneuver enabled by collision-resilient quadrotors to decelerate and achieve a sudden change in momentum. A set of 60 flight experiments using the recovery controller from Section III-B were performed to create a collision model for XPLORER in various scenarios to predict the post-collision state. It is seen that for a large range of velocities from magnitudes $0\text{-}1.5 \text{ m/s}$, the post-collision velocities can drop to very low values of around 0.3 m/s without much control effort for braking (collide-to-brake/collide-to-decelerate). This observation, enables us to generate new ricocheting maneuvers for the passive collision-resilient quadrotors such as XPLORER. We show via experiments that exploiting maneuvers with $\Gamma = 4$ in which the UAV collides and loses almost all kinetic energy leads to interesting ricocheting maneuvers that compliant UAVs can demonstrate efficiently. Therefore, to achieve the minimum time trajectory, we choose the maximum velocity that XPLORER can

physically attain and demonstrate ricocheting maneuvers for reaching to goal in minimum time as discussed in the results Section V-E.

V. RESULTS AND DISCUSSION

A. Experimental Setup, Sensors and Control Parameters

1) *Hardware, Software, and Physical Setup*: The flight controller utilized is a PIXHAWK flight controller with the Raspberry Pi 4 B as the companion computer. The high-level companion computer is used to relay the position and orientation data from the indoor motion capture system to the flight controller at 120 Hz . A 4S lithium polymer battery of 3300 mAh LiPo battery of 14.8 V , 50 C is used for the power supply. The motors are controlled utilizing Lumenier 30A BLHeli_S Electronic Speed Controllers and the entire system has a mass of 1.12 kg . To validate the performance of the algorithms, XPLORER was tested in four distinct environments- (i) a rectangular object measuring $1.22 \text{ m} \times 1.0 \text{ m}$ was set up using acrylic panels (ii) acrylic panels were organized to represent a box with XPLORER's initial state outside the box (iii) a trash can and (iv) a vertical pipe to represent real obstacles.

2) *Sensors, Measurements for arm and CoM-based force/torque estimates*: We employ low-cost off-the-shelf inertial measurement units (IMUs) on each arm to measure acceleration and estimate the external force on the arm. IMUs were employed due to their low costs, lightweight, strong resilience, and easy integration, compared to other sensors such as encoders. Accordingly, four 9-DOF IMUs (BNO055, Adafruit, New York, NY) are mounted on XPLORER (one on each arm) and are connected to the RaspberryPI via serial communication at 50 Hz . The Euler angles are computed using the Adafruit BNO055 library. A median low-pass with a band-stop filter is employed to obtain accurate estimates of the arm angles, θ_i , at any given instant. For the system identification, the inertia about z -axis for the arm, \mathcal{J}_{zz} was calculated using SolidWorks to be 0.0015 kgm^2 . We design an experiment where the base of the XPLORER is held by a clamp and the torsional spring-based arm is first loaded to a certain fixed position using a force sensor. Then it is released and the motion capture system is used to generate the trajectory of the arm. We then use the MATLAB System ID toolbox to obtain the b and k values as 0.009 and 1.307 for $\mathcal{J}_{zz} = 0.0015 \text{ kgm}^2$ in (3).

3) *Thrust Estimate and Parameters of Interaction Controller*: In order to calculate the wrench at the CoM, the controller's normalized force and torque values are obtained from the onboard flight controller. The force value is scaled by a factor of 32.5 to generate the required thrust, which is obtained empirically by calculating the hover thrust, and used to calculate the approximate value of the actual thrust. This technique can be significantly improved by performing a PWM-thrust mapping curve using RPM feedback. Gains for the interaction controller (8) are tuned by experiments to be:

$$D = \begin{bmatrix} 24.5 & 0 & 0 & 0 \\ 0 & 24.5 & 0 & 0 \\ 0 & 0 & 0 & 0 \\ 0 & 0 & 0 & 1 \end{bmatrix}, K = \begin{bmatrix} 24.5 & 0 & 0 & 0 \\ 0 & 24.5 & 0 & 0 \\ 0 & 0 & 0 & 0 \\ 0 & 0 & 0 & 1 \end{bmatrix}, m_v = \mathcal{I}_{v,z} = 1$$

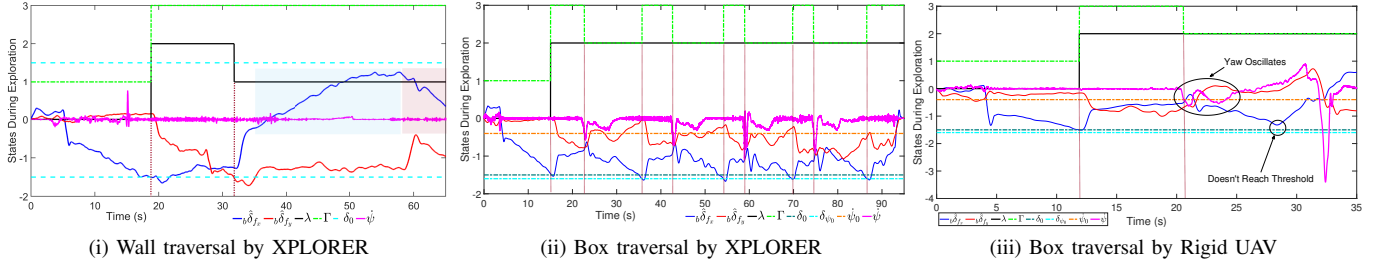


Fig. 5. (i) shows the results for the exploration with XPLOER of a wall-like structure. The exploration states are triggered when the threshold for δ_0 is crossed. In this case, only two states corresponding to $\Gamma = 1$ and 3 are activated. The blue and red regions indicate the presence of unmodeled frictional and wall-effects (ii) shows the results for the exploration of a box-like structure. The exploration states are switched when the thresholds for δ_0 or ψ_0 are crossed. In this case, all three states corresponding to $\Gamma = 1, 2, 3$ are activated. The top view of the experiments is shown in Fig.6. (iii) shows the results of the exploration of rigid UAV for convex corners. The rigid UAV tries to yaw, however, due to the high interaction force required for maintaining the turning maneuver and the absence of compliance in the chassis brings about oscillatory yaw motion, failing to engage *Tactile-traversal* after *Tactile-turning*.

B. Static Wrench Application

The results for a static wrench application task are shown in Fig. 4(i). The reference for this experiment is set to $\delta_{f_{ref}} = [-1 \ 0 \ 0]^T$ for applying a 1 N force on the wall. In order to validate the force estimates obtained from our proposed method, we use a load cell (ATO Micro 5kg Tension and Compression Load Cell, S Type, ATO, Diamond Bar, CA) mounted on the wall. A digital reader is attached to the load cell which is calibrated to display the force readings when the load cell is compressed. The UAV takes off and starts applying force on the box whose other end pushes the load cell. The sampling rate of the sensor is 20 Hz, hence it is noted that the force values settle to its set desired force value. A video of the experimental setup is available in Supplementary Video 7.

The insets in Figs. 4 shows the deviation of the arm angles used to calculate the arm wrench ${}^w\hat{\delta}_{f_{a_i}}$. The dotted magenta line shows the actual force measured by a force sensor set up on the wall at a steady state. The estimate from the CoM (blue dotted line) takes time to converge, however, the arm-based force estimate converges sooner without the collision peak. By fusing both methods, the proposed estimator retains the peak from the CoM-based method and also converges faster. For this experiment, the true force applied on the wall after settling was measured to be approximately 1.3 N using a force sensor as shown by the dashed magenta line, demonstrating an accuracy of 0.3N for this task.

C. Autonomous Tactile-based Exploration

We describe the validation of the exploratory algorithm proposed in Section IV-A for a wall-like and box-like structure. A moving average filter with 50 samples is employed to filter ${}_b\hat{\delta}_f$, while a low-pass filter is utilized to eliminate noise in the yaw rate, ψ . This is done to ensure that the state machine Γ is failsafe to noise perturbations.

The state machine for XPLOER relies on several parameters that require fine-tuning through trials. After extensive testing, we have determined the optimal values for these parameters that work well in all environments, and they are listed in Table 2. To prevent excessive force on the objects in the environment and considering flight time, we limited δ_0 to 1.5 N, though it is capable of exerting forces greater than 2 N. Furthermore, as XPLOER approaches right-angled corners/edges and rotates around those points, the corresponding yaw rate is measured to be 0.6 rad/s, which correlates to the

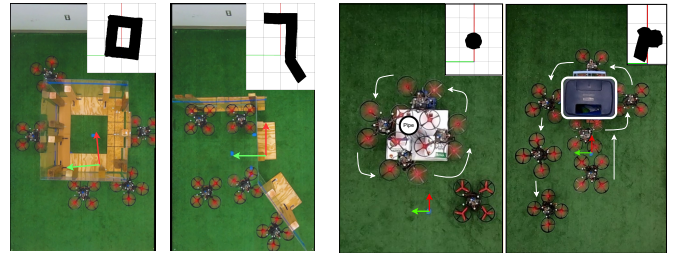


Fig. 6. Top view of the experiments with the corresponding maps generated by the algorithm in the insets. Left to right: a closed box-like structure, a wall-like structure, an acrylic pipe and a trash can.

force of 1.5 N being applied. Any increase in the applied force will result in a higher yaw rate. We choose 0.4 rad/s to detect such a maneuver. For the *Tactile-turning* state, the controlled yaw maneuver is performed at 0.26 rad/s.

1) *Wall-traversal by XPLOER*: XPLOER takes off and upon reaching a hover height of 0.7 m, it switches to *Exploration* state and moves in the positive x direction in the body frame. Once it detects the threshold external wrench, δ_0 in its movement direction, it switches to the *Tactile-traversal* state as described in Section IV-A. It maintains contact with the obstacle by applying f_{des} force and moves across the environment. Throughout the flight, the yaw is in admittance ensuring two arms of the UAV are in contact with the obstacle. In this experiment the *Exploration* and *Tactile-traversal* states are predominantly used for the navigation as shown in Fig. 5i and is shown in Supplementary Video 2.

2) *Box-traversal by XPLOER*: First the exploration algorithm described in the above section is initiated. Upon reaching a hover height of 0.7 m, XPLOER switches to *Exploration* state and moves in the positive x direction in the body frame. Upon encountering the wall, it proceeds to move across the obstacle until it reaches the corner where it releases and yaws. This triggers the *Tactile-turning* state which allows it to yaw in a controlled manner and establish contact with the adjacent wall, effectively switching back to the *Tactile-traversal* state. It continues traversing all the edges until it returns to the initial contact position, thereby achieving loop closure. From Fig. 5ii we can infer that all three states corresponding to $\Gamma = 1, 2$ and 3 are activated whilst circumnavigating the obstacle.

3) *Trash can and Pipe-traversal by XPLOER*: Additional results for exploration of real-world objects such as a trash can

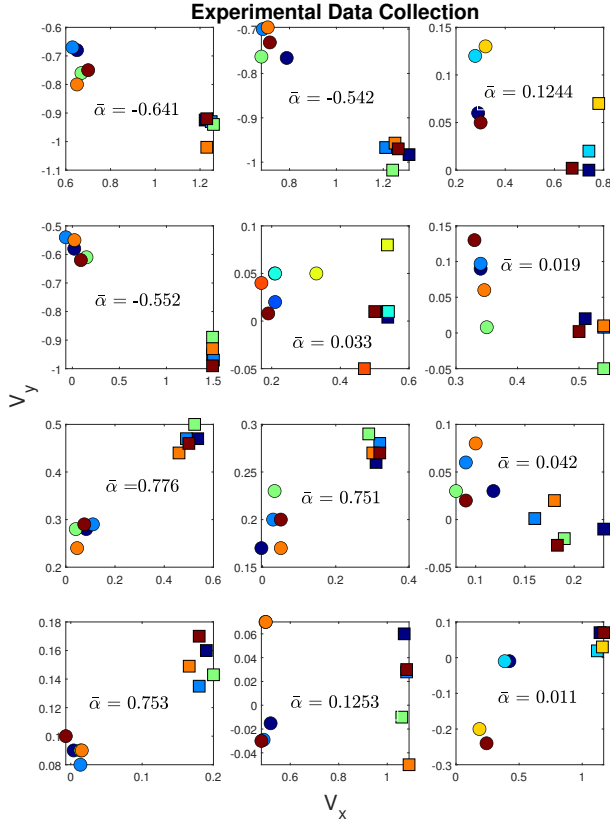


Fig. 7. A set of sixty experiments to model the post-collision velocities for designing the ricocheting primitive. The x -axis and y -axis denote the x and y direction velocities respectively. Symbols \square and the \circ represent the pre and post-collision velocities for each color. $\bar{\alpha}$ represents the mean heading direction to the collision surface.

and pipe gave consistent performance showing the accuracy of the proposed tactile-exploration strategy for real-world objects.

4) *Comparison against a Rigid UAV*: We conducted both wall-traversal and box-traversal experiments for a similar dimension rigid UAV and only the wall-traversal exploration with concave edges was successful. As shown in the Fig. 5iii, for a convex outer edge box-like obstacle, after initial contact and desired force application, the state machine moves to *Tactile-turning* upon detecting a high yaw-rate. However, due to the absence of the spring-damper action, during this turning, significant oscillations are observed in yaw and the UAV was not able to maintain contact and apply the desired force during turning, thereby unable to move to the tactile-traversal state again. The same observations are made in all four experiments conducted for this case. As a result, the exploration for a rigid drone failed in all four trials conducted for a box-like exploration. Furthermore, sometimes whenever the rigid UAV makes an impact, due to the high rebound velocities, and the presence of yaw admittance control given by (8), there is a high yaw-rate which falsely triggers the *Tactile-turning* state as shown in Fig. 5iii and the tactile-exploration scheme fails.

D. Mapping

The hyperparameter δ_{map} is set to 1.51 N to ensure that the mapping is initiated only when the vehicle has firm contact with the obstacle. Furthermore, an additional check ensures that mapping is conducted only when XPLORER is flying. The

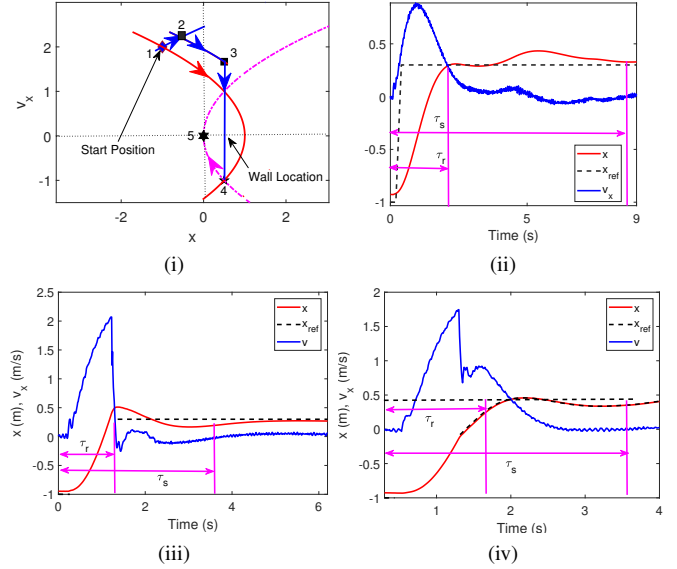


Fig. 8. (i) Simulation results and the phase-portrait for the proposed collision-inclusive state-jumps - ricocheting. (ii) Experimental results for a case without collision, with $\tau_r = 2.27$ and $\tau_s = 8.995$ seconds. (iii) Experimental results for the ricocheting ($\Gamma = 4$) and stop exactly near wall, $\tau_r = 1.046$ and $\tau_s = 5.292$ seconds (iv) Experimental results for $\Gamma = 4$ to stop beyond wall, $\tau_r = 1.685$ and $\tau_s = 3.631$ seconds.

generated map allows for the measurement of the dimension of the box, which is 1.231 m \times 1.019 m and the actual dimensions are 1.22 m \times 1.0 m. The accuracy is about 96.72% for computing the area of the box. One source of the mapping error is the imperfect position estimation (small errors from the motion capture system in our experiment), as it propagates in state estimation and to the point cloud data. The results are also shown in Supplementary Video 3.

Furthermore, the map of the environment as generated by the proposed algorithm is shown in the insets of Fig. 6 for the four objects of a box-like structure, inside wall-boundary traversal, pipe, and a trash can respectively.

E. Waypoint Tracking via Ricocheting

The 60 flight data points for post-collision behavior prediction are shown in Fig. 7 and the advantages of utilizing ricocheting to get velocity state-jumps is first shown via simulations in Fig. 8i. Without ricocheting, path 1-2-3-4-5 would have been followed, however, with ricocheting, path 1-2-4-5 is feasible with a shorter flight time [40]. We also demonstrate the benefits of ricocheting via three experiments. In the first case, no ricocheting is performed, in the second case the goal is near the wall to facilitate ricocheting off the wall's face, and in the third case, the goal position is set some distance beyond the wall to enable ricocheting off the edge.

The rise time (τ_r) and the settling time (τ_s) are chosen as the metrics to evaluate the performance of ricocheting. Comparison with the conventional, collision-exclusive trajectory is shown in Fig. 8ii. In this case, the vehicle first reaches the setpoint, overshoots, and then tries to minimize the error by slowly converging to the reference. The τ_r and τ_s are noted to be 2.27 and 8.995 seconds, respectively. Furthermore, over three trials the RMSE error was around ± 3 cm for this case. In contrast, the experimental results for ricocheting show that

XPLORER reaches the wall with maximum velocity, collides, and stops at the wall almost instantaneously by dissipating kinetic energies as shown by the plots in Fig. 8iii. The τ_r and τ_s are calculated to be 1.046 and 5.292 seconds, respectively which are faster than the conventional trajectories. For the case where the vehicle performs ricocheting and regulates itself to a setpoint beyond the wall, and results in Fig. 8iv show significantly shorter convergence time with $\tau_r = 1.685$ seconds and $\tau_s = 3.631$ seconds, respectively. The low settling time for the later case as compared to a sudden stop at the wall can be attributed to the wall effect which affects the performance of the vehicle for the ricocheting case as also noted in Section V-A3. We also noted that the RMSE values over 6 trials for the collision-inclusive trajectories were $\pm 0.5\text{cm}$ showing improved tracking accuracy than the conventional maneuvers. This can be attributed to the dissipation of kinetic energies upon collision, leading to improved decelerating performance. All the experimental results for ricocheting are shown in Supplementary Video 4.

VI. CONCLUSION

In this work, we presented a complete autonomous exploration, navigation, and control framework for a passive deformable quadrotor, XPLORER, for exploring unknown environments through contact. An external force estimation algorithm was proposed using proprioceptive information and was successfully verified by experiments. Furthermore, the autonomous exploration and mapping scheme was shown to successfully explore unknown flight spaces. Finally, a novel ricocheting maneuver was introduced which generated minimum-time paths by exploiting collision-induced state jumps. Future work will look into collision location isolation for improved wrench estimates and design of onboard fast motion planning algorithms by leveraging the proposed motion-primitives.

VII. ACKNOWLEDGMENTS

The authors thank the ASU RISE lab members, Bill Nguyen and Yogesh Kumar, for their help with experiments.

REFERENCES

- [1] F. Ruggiero *et al.*, "Aerial manipulation: A literature review," *IEEE Robot. Autom. Lett.*, vol. 3, no. 3, pp. 1957–1964, 2018.
- [2] D. Hausamann *et al.*, "Monitoring of gas pipelines—a civil uav application," *Aircraft Eng. Aero. Tech.*, vol. 77, no. 5, pp. 352–360, 2005.
- [3] S. Mishra *et al.*, "Autonomous vision-guided object collection from water surfaces with a customized multirotor," *IEEE/ASME Trans. Mech.*, vol. 26, no. 4, pp. 1914–1922, 2021.
- [4] S. Kim *et al.*, "Aerial manipulation using a quadrotor with a 2dof robotic arm," in *IEEE/RSJ Int. Conf. Intl. Robot. Sys.*, pp. 4990–4995, 2013.
- [5] A. Suarez *et al.*, "Lightweight compliant arm for aerial manipulation," in *IEEE/RSJ Int. Conf. Intl. Robot. Sys.*, pp. 1627–1632, 2015.
- [6] M. Kovac, "Learning from nature how to land aerial robots," *Science*, vol. 352, no. 6288, pp. 895–896, 2016.
- [7] S. Mintchev and D. Floreano, "Adaptive morphology," *IEEE Robot. Autom. Mag.*, vol. 23, no. 3, pp. 42–54, 2016.
- [8] H. Suh *et al.*, "Energy-efficient motion planning for multi-modal hybrid locomotion," in *IEEE/RSJ Int. Conf. Intl. Robot. Sys.*, pp. 7027–7033, 2020.
- [9] K. Patnaik and W. Zhang, "Towards reconfigurable and flexible multi-rotors," *Int. J. Intel. Robot. App.*, vol. 5, no. 3, pp. 365–380, 2021.
- [10] K. Patnaik *et al.*, "Design and control of squeeze," in *IEEE/RSJ Int. Conf. Intl. Robot. Sys.*, pp. 1364–1370, 2020.
- [11] Z. Liu and K. Karydis, "Toward impact-resilient quadrotor design, collision characterization and recovery control to sustain flight after collisions," in *IEEE Int. Conf. Robot. Autom.*, pp. 183–189, 2021.
- [12] K. Patnaik *et al.*, "Collision recovery control of a foldable quadrotor," in *IEEE/ASME Int. Conf. Adv. Intl. Mech.*, pp. 418–423, 2021.
- [13] P. H. Nguyen, K. Patnaik, *et al.*, "A soft-bodied aerial robot for collision resilience and contact-reactive perching," *Soft Robotics*, 2023.
- [14] V. Serbezov *et al.*, "Application of multi-axis force/torque sensor system," *IOP Conf. Mater. Sci. and Eng.*, vol. 878, no. 1, p. 012039, 2020.
- [15] A. Ollero *et al.*, "The aeroarms project," *IEEE Robot. Autom. Mag.*, vol. 25, no. 4, pp. 12–23, 2018.
- [16] F. Ruggiero *et al.*, "Impedance control of vtol uavs with a momentum-based external generalized forces estimator," in *IEEE Int. Conf. Robot. Autom.*, pp. 2093–2099, 2014.
- [17] F. Ruggiero *et al.*, "Passivity-based control of vtol uavs with a momentum-based estimator of external wrench and unmodeled dynamics," *Robot. Auto. Sys.*, vol. 72, pp. 139–151, 2015.
- [18] B. Yüksel *et al.*, "A nonlinear force observer for quadrotors and application to physical interactive tasks," in *IEEE/ASME Int. Conf. Adv. Intl. Mech.*, pp. 433–440, 2014.
- [19] M. Ryll *et al.*, "6d interaction control with aerial robots: The flying end-effector paradigm," *Int. J. Robot. Research*, vol. 38, no. 9, pp. 1045–1062, 2019.
- [20] C. D. McKinnon and A. P. Schoellig, "Unscj external force and torque estimation for quadrotors," in *IEEE/RSJ Int. Conf. Intl. Robot. Sys.*, pp. 5651–5657, 2016.
- [21] T. Tomić *et al.*, "External wrench estimation, collision detection, and reflex reaction for flying robots," *IEEE Trans. Robot.*, vol. 33, no. 6, pp. 1467–1482, 2017.
- [22] P. Pfändler *et al.*, "Flying corrosion inspection robot for corrosion monitoring of civil structures—first results," in *SMAR Conf. on Smart Moni. Assess. Rehab. Civil Struc. Prog.*, pp. We–4, 2019.
- [23] J. Hu, S. Zhang, E. Chen, and W. Li, "A review on corrosion detection and protection of existing reinforced concrete (rc) structures," *Construction and Building Materials*, vol. 325, p. 126718, 2022.
- [24] K. Alexis *et al.*, "Aerial robotic contact-based inspection: planning and control," *Autonomous Robots*, vol. 40, pp. 631–655, 2016.
- [25] K. Bodie *et al.*, "Active interaction force control for contact-based inspection with a fully actuated aerial vehicle," *IEEE Trans. Robot.*, vol. 37, no. 3, pp. 709–722, 2020.
- [26] M. Tognon *et al.*, "A truly-redundant aerial manipulator system with application to push-and-slide inspection in industrial plants," *IEEE Robot. Autom. Lett.*, vol. 4, no. 2, pp. 1846–1851, 2019.
- [27] B. Brogliato, *Nonsmooth mechanics*, vol. 3. Springer, 1999.
- [28] J.-C. Zufferey, A. Beyeler, and D. Floreano, "Optic flow to steer and avoid collisions in 3d," *Flying Insects and Robots*, pp. 73–86, 2010.
- [29] D. Schafroth, S. Bouabdallah, C. Bermes, and R. Siegwart, "From the test benches to the first prototype of the muffy micro helicopter," *J. Intel. Robot. Sys.*, vol. 54, pp. 245–260, 2009.
- [30] R. He, A. Bachrach, and N. Roy, "Efficient planning under uncertainty for a target-tracking micro-aerial vehicle," in *IEEE Int. Conf. Robot. Autom.*, pp. 1–8, 2010.
- [31] S. Shen, N. Michael, and V. Kumar, "Autonomous multi-floor indoor navigation with a computationally constrained mav," in *IEEE Int. Conf. Robot. Autom.*, pp. 20–25, 2011.
- [32] D. Scaramuzza *et al.*, "Vision-controlled micro flying robots," *IEEE Robot. Autom. Mag.*, vol. 21, no. 3, pp. 26–40, 2014.
- [33] N. Khedekar *et al.*, "Contact-based navigation path planning for aerial robots," in *Int. Conf. Robot. Autom.*, pp. 4161–4167, IEEE, 2019.
- [34] P. De Petris *et al.*, "Resilient collision-tolerant navigation in confined environments," in *IEEE Int. Conf. Robot. Autom.*, pp. 2286–2292, 2021.
- [35] J. Zha and M. W. Mueller, "Exploiting collisions for sampling-based multicopter motion planning," in *IEEE Int. Conf. Robot. Autom.*, pp. 7943–7949, 2021.
- [36] J. L. Schonberger and J.-M. Frahm, "Structure-from-motion revisited," in *Proc. IEEE Conf. Comput. Vis. Patt. Recog.*, pp. 4104–4113, 2016.
- [37] D. Cattaneo *et al.*, "Cmnet: Camera to lidar-map registration," in *IEEE Intel. Transp. Sys. Conf.*, pp. 1283–1289, 2019.
- [38] K. M. Hasan, K. J. Reza, *et al.*, "Path planning algorithm development for autonomous vacuum cleaner robots," in *Int. Conf. Info. Elec. Vis.*, pp. 1–6, IEEE, 2014.
- [39] Q.-Y. Zhou, J. Park, and V. Koltun, "Open3D: A modern library for 3D data processing," *arXiv:1801.09847*, 2018.
- [40] A. Cristofaro *et al.*, "Time-optimal control for the hybrid double integrator with state-driven jumps," in *IEEE Conf. Decision. Control*, pp. 6301–6306, 2019.